Gardiner, S. H., Karsili, T. N. V., Lipciuc, M. L., Wilman, E., Ashfold, M. N. R., & Vallance, C. (2014). Fragmentation dynamics of the ethyl bromide and ethyl iodide cations: a velocity-map imaging study. *Physical Chemistry Chemical Physics*, *16*(5), 2167-2178. https://doi.org/10.1039/c3cp53970a

Journal Name

Dynamic Article Links ►

Cite this: DOI: 10.1039/c0xx00000x

www.rsc.org/xxxxxx

ARTICLE TYPE

Fragmentation dynamics of the ethyl bromide and ethyl iodide cations: a velocity-map imaging study

Sara H. Gardiner[a], Tolga N.V. Karsili[b], M. Laura Lipciuc[a], Edward Wilman[a], Michael N.R. Ashfold[b], and Claire Vallance[a]

[a] Department of Chemistry, University of Oxford, Chemistry Research Laboratory, 12 Mansfield Rd, Oxford OX1 3TA, UK; [b] School of Chemistry, University of Bristol, Cantock's Close, Bristol BS8 1TS, UK

Received (in XXX, XXX) Xth XXXXXXXXX 20XX, Accepted Xth XXXXXXXXX 20XX
DOI: 10.1039/b000000x

The photodissociation dynamics of ethyl bromide and ethyl iodide cations ($C_2H_5Br^+$ and $C_2H_5I^+$) have been studied. Ethyl halide cations were formed through vacuum ultraviolet (VUV) photoionization of the respective neutral parent molecules at 118.2 nm, and were photolysed at a number of ultraviolet (UV) photolysis wavelengths, including 355 nm and wavelengths in the range from 236 to 266 nm. Time-of-flight mass spectra and velocity-map images have been acquired for all fragment ions and for ground (Br) and spin-orbit excited (Br*) bromine atom products, allowing multiple fragmentation pathways to be investigated. The experimental studies are complemented by spin-orbit resolved *ab initio* calculations of cuts through the potential energy surfaces (along the $R_{C-Br/I}$ stretch coordinate) for the ground and first few excited states of the respective cations. Analysis of the velocity-map images indicates that photoexcited $C_2H_5Br^+$ cations undergo prompt C–Br bond fission to form predominantly $C_2H_5^+$ + Br* products with a near-limiting 'parallel' recoil velocity distribution. The observed $C_2H_3^+ + H_2$ + Br product channel is thought to arise via unimolecular decay of highly internally excited $C_2H_5^+$ products formed following radiationless transfer from the initial excited state populated by photon absorption. Broadly similar behaviour is observed in the case of $C_2H_5I^+$, along with an additional energetically accessible C–I bond fission channel to form $C_2H_5 + I^+$ products. HX (X = Br, I) elimination from the highly internally excited $C_2H_5X^+$ cation is deemed the most probable route to forming the $C_2H_4^+$ fragment ions observed from both cations. Finally, both ethyl halide cations also show evidence of a minor C–C bond fission process to form $CH_2X^+ + CH_3$ products.

1. Introduction

Methyl iodide (CH_3I) has long been regarded as a benchmark molecule for understanding the photodissociation dynamics of polyatomic molecules.[1-15] Studies carried out on timescales spanning the nanosecond to femtosecond range have yielded insights into energy partitioning, interactions between excited states, product angular momentum polarisation, and a range of other phenomena. Starting with the first demonstration of ion imaging by Chandler and Houston in 1987,[8] methyl iodide has also proven to be a popular molecule for demonstrating new experimental imaging methods in chemical dynamics, and has been widely studied by velocity-map imaging (VMI) and related techniques.[10-13] Unsurprisingly, interest has extended to the photodynamics of other methyl halides (CH_3X), and there have been several studies on CH_3Cl, CH_3Br, and CH_3I in both their neutral (see [16] and references therein) and cationic forms[17-24]; these earlier studies provide a valuable point of reference for the present investigations into the photofragmentation of two ethyl halide cations, $CH_3CH_2Br^+$ and $CH_3CH_2I^+$.

In the case of neutral CH_3X, the primary dissociation channel following excitation at UV wavelengths is C–X bond fission to form a methyl radical with a with a ground or spin-orbit excited halogen atom co-fragment (henceforth represented as X and X*), CH_3 + X/X* (see [9-11,25,26] and references therein). C–X bond fission is also the dominant dissociation pathway following photoexcitation of CH_3X^+ cations at low photon energies (≤ 4 eV), leading to production of a methyl cation with a halogen co-fragment, CH_3^+ + X/X*.[19-22,27] The alternative C–X bond fission channel yielding $CH_3 + X^+$ fragments opens at higher excitation energies.[18] The observed fragmentation behaviours of both neutral and cationic methyl halide species have been rationalised in terms of the excited electronic states accessible upon photoexcitation, and the way in which their respective potential energy surfaces (PESs) correlate with the available dissociation limits. The ground ($^2E_{3/2}$) and first excited ($^2E_{1/2}$) states of CH_3X^+ correlate with CH_3^+ + X products. In the case of CH_3Br^+, the

next lowest lying dissociation limit involves CH_3^+ + Br* products, whereas for CH_3I^+, the larger spin-orbit splitting in atomic iodine relative to atomic bromine results in the CH_3 + I^+ limit lying below that for forming CH_3^+ + I* products[19,23,24].

Previous photoexcitation studies involving ethyl halide cations, $C_2H_5X^+$, have identified the analogous C–X bond fission channels and several additional pathways, each of which results in one singly charged species and one or more neutral fragments. In the cases of $C_2H_5Br^+$ and $C_2H_5I^+$, photoelectron-photoion coincidence (PEPICO) methods have been used to study fragmentation processes yielding $C_2H_5^+$ ions following excitation at energies ≤3 eV above the respective C–X bond dissociation limits[28,29]. More recently, these same $C_2H_5X^+$ cations have been employed in determinations of the enthalpy of formation of $C_2H_5^+$.[30,31] Additionally, Tang *et al.*[32] have reported images of I^+ fragments formed following one-colour multiphoton excitation of C_2H_5I at wavelengths λ ≤ 266 nm. These products were plausibly attributed to one-photon dissociation of $C_2H_5I^+$ cations that were themselves formed by two-photon excitation (via the A band) of C_2H_5I. Apart from this study, we are not aware of any other photofragment imaging studies of the ethyl iodide cation. Xu et al.[33] have reported a detailed photolysis study of $C_2H_5Br^+$ cations at one wavelength (355 nm), including data from time-of-flight (TOF) mass spectrometry, and velocity-map imaging of the observed fragment ions, and discussion of their possible formation pathways. These authors refute an earlier suggestion that $C_2H_5^+$ fragments are formed via an ion pair mechanism following 118 nm excitation of C_2H_5Br.[34] Here we report: (i) a much more detailed analysis of the photofragmentation of $C_2H_5Br^+$ cations than reported hitherto, based on measurements with sufficient mass resolution to allow distinction between channels yielding, for example, $C_2H_5^+$, $C_2H_4^+$ and $C_2H_3^+$ fragment ions; and (ii) the first detailed investigations into the multiple photodissociation pathways available to $C_2H_5I^+$ cations. The fragmentation dynamics are probed as a function of UV excitation wavelength at one or more wavelengths in the range 236-266 nm and at 355 nm.

2. Methods

2.1 Experiment

Photofragment velocity-map images were recorded using a custom-built VMI spectrometer, which has been described in detail previously.[35] A gas mixture comprising ~1% ethyl bromide (bromoethane, Sigma Aldrich, >99%) or ethyl iodide (iodoethane, Sigma Aldrich, >99%) seeded in 2 bar He (BOC, >99.9%) was expanded through a pulsed solenoid valve (Parker Hannifin Series 9) at a repetition rate of 10 Hz. The resulting pulsed molecular beam passed through a skimmer into the imaging chamber, and was intersected at right angles within the VMI optics assembly by the VUV ionization and UV photolysis laser radiation.

VUV light of wavelength 118.2 nm (hereafter referred to as 118 nm) was produced by tripling the 354.7 nm (hereafter referred to as 355 nm) third harmonic of a Nd:YAG laser (Continuum Surelite I, ~10-20 mJ per 5 ns pulse) in a phase-matched Xe/Ar gas mixture.[36-39] The 355 nm laser beam was tightly focused into a gas cell containing a mixture of Xe (BOC, >99.9%) and Ar (BOC, >99.9%) in a ratio of 1:11. The 118 nm and residual 355 nm light were not separated before entering the imaging chamber, and in some of the experiments the latter was used to effect photolysis of the parent cation of interest. In all other 'two-laser' experiments, the requisite UV photolysis light (in the wavelength range 236-266 nm) was produced using a tuneable, frequency-doubled, pulsed dye laser (Sirah Cobra Stretch, 7 ns pulse, laser energy < 0.4 to 1 mJ/pulse in a 1×1 mm^2 spot size in the interaction region, $\Delta\nu \approx 0.3$ cm^{-1}) which was pumped by the third harmonic of a Nd:YAG laser (Continuum Surelite II, 200 mJ per 7 ns pulse). All laser beams were linearly polarised, with their respective electric field vectors, **ε**, aligned parallel to the plane of the imaging detector.

During an experimental cycle, the 118 nm radiation was used to ionize the ethyl halide of interest, and the UV light then photolysed the resulting ion. All two-laser studies employed a short time delay of ~20 ns between the ionization and photolysis pulses, whereas in the 355 nm photolysis studies, the two pulses were coincident in time. $C_2H_5Br^+$ and $C_2H_5I^+$ photolysis was investigated at 355 nm and 266 nm, with addition studies at 248 nm and 236 nm for $C_2H_5I^+$. Given the temporal coincidence of the 355 nm and 118 nm pulses, we recognise that the 'one-laser' images could, in principle, contain contributions from 355 nm photolysis of the neutral ethyl halide followed by 118 nm ionization of the resulting fragments. No electronic states of either of the neutral parent molecules are accessed by one photon absorption at 355 nm, however, and the absorption cross-sections at 355 nm are therefore negligible compared to those at 118 nm. Given this, and the evident similarities between the one and two-laser images, we concur with the conclusions reached by Xu *et al.*[33] that the one-laser experiments do indeed probe 355 nm photolysis of $C_2H_5X^+$ cations formed by 118 nm photoionization, and include the results of such studies here along with those from the two-laser experiments.

As noted earlier, $C_2H_5X^+$ photolysis yields one ionic and at least one neutral fragment. Neutral halogen atoms can be detected via resonance-enhanced multiphoton ionization (REMPI),[40-43] which is readily achieved in the present VMI spectrometer by focusing the frequency-doubled dye laser output (of an appropriate wavelength) into the interaction region. This method is employed here for detecting Br and Br* fragments, using wavelengths of 266.64 nm and 266.70 nm, resonant with the $4p^45p(^4P^o_{3/2})\leftarrow 4p^5(^2P^o_{3/2})$ and $4p^45p(^4S^o_{3/2})\leftarrow 4p^5(^2P^o_{1/2})$ two photon transitions, respectively.[8,43,44]

The ions were extracted through a 482 mm field-free region and velocity-map imaged onto a 40 mm position-sensitive ion detector (Photonis) consisting of a chevron pair of microchannel plates (MCPs) coupled to a P47 phosphor screen. To identify the ions formed in a given experiment, time-of-flight mass spectra (TOF-MS) were recorded by stepping a 20 ns time gate across the range of arrival times of interest and logging the total ion signal recorded by the camera at each arrival time. The TOF-MS revealed the arrival times for the fragment and parent ions and showed no evidence of cluster formation. Images were then acquired for the arrival times corresponding to ions of interest. In order to achieve selective detection of one specific ion, the voltage applied to the back MCP was pulsed on at the appropriate arrival time by applying a +500 V pulse from a high-speed MCP

time-gating module (Photek, GM-MCP-2). The image generated at the phosphor screen was captured by an intensified CCD camera (Photonic Science MiniIDI), and images were thresholded frame-by-frame and accumulated on a PC *via* a LabView interface. Images were typically acquired over several tens of thousands of laser shots in order to achieve a sufficiently good signal-to-noise ratio. Images from photolysis at wavelengths other than 355 nm were obtained by successively recording the necessary 'two-laser' and 'one-laser' images and subtracting as appropriate. The images were processed using a polar onion peeling algorithm in order to extract the central slice through the three-dimensional photofragment velocity distribution,[45] from which the product translational energy distribution could be determined. Total translation energies, E_T, are obtained by scaling the experimentally derived kinetic energy of the monitored fragment ion ($Frag^+$) by the mass factor $m_{C_2H_5X} / (m_{C_2H_5X} - m_{Frag})$.

2.2 Computational methodology

The Gaussian 09[46] computational package was used to optimise the geometry of ground state $C_2H_5I^+$ and $C_2H_5Br^+$ cations using Møller-Plesset second order perturbation theory (MP2) with the LANL2D basis set.

Rigid-body potential energy curves (PECs) along the $R_{C–I}$ and $R_{C–Br}$ coordinates were calculated for both cations with the rest of the nuclear framework fixed at the ground state MP2 equilibrium geometry. C_S symmetry (of the heavy atom chain) was maintained throughout these rigid-body scans. Spin-orbit free PECs were calculated using a state-averaged (SA) CASSCF reference wavefunction involving the first three ^{2}A' and ^{2}A" states, and the first ^{4}A' and ^{4}A" states. The energies of all states were calculated using a complete active space with second order perturbation theory (CASPT2) and the SA-CASSCF reference wavefunction. An imaginary level shift of 0.5 a.u. was used in all CASPT2 calculations to encourage convergence and to eliminate intruder state effects. The Dunning's cc-pVTZ contracted correlation-consistent basis set was assigned to all atoms in both the SA-CASSCF and CASPT2 calculations. A 46 electron relativistic effective core potential[47], along with the larger cc-pVTZ-pp basis of Peterson *et al.*[48] was used to treat the I atom. An active space consisting of 6 electrons in 4 orbitals (the two halogen centred p_x out-of-plane and p_y in-plane orbitals, and the C–X bond centred σ and σ* orbitals) was used for these calculations.

Spin-orbit-coupled states were then calculated by evaluating $\hat{H}_{SO}$ in a basis of ψ_{elec}; these states are henceforth labelled using the extended irreducible representation including both spin-orbit-free and spin parts. CASPT2 (rather than CASSCF) energies of the spin-orbit-free states were used in the diagonalisation of the spin-orbit coupling matrix in order to allow for some treatment of dynamic correlation. As shown below, such rigid body scans are useful in understanding the various parent cation to photoproduct correlations, but are of limited energetic value. In particular, the geometry of the ground state $C_2H_5^+$ cation is very different from that of the ethyl radical or of the ethyl group in the parent cation,[49,50] so the CASPT2 calculations substantially overestimate the C–X bond strength in the parent cation.

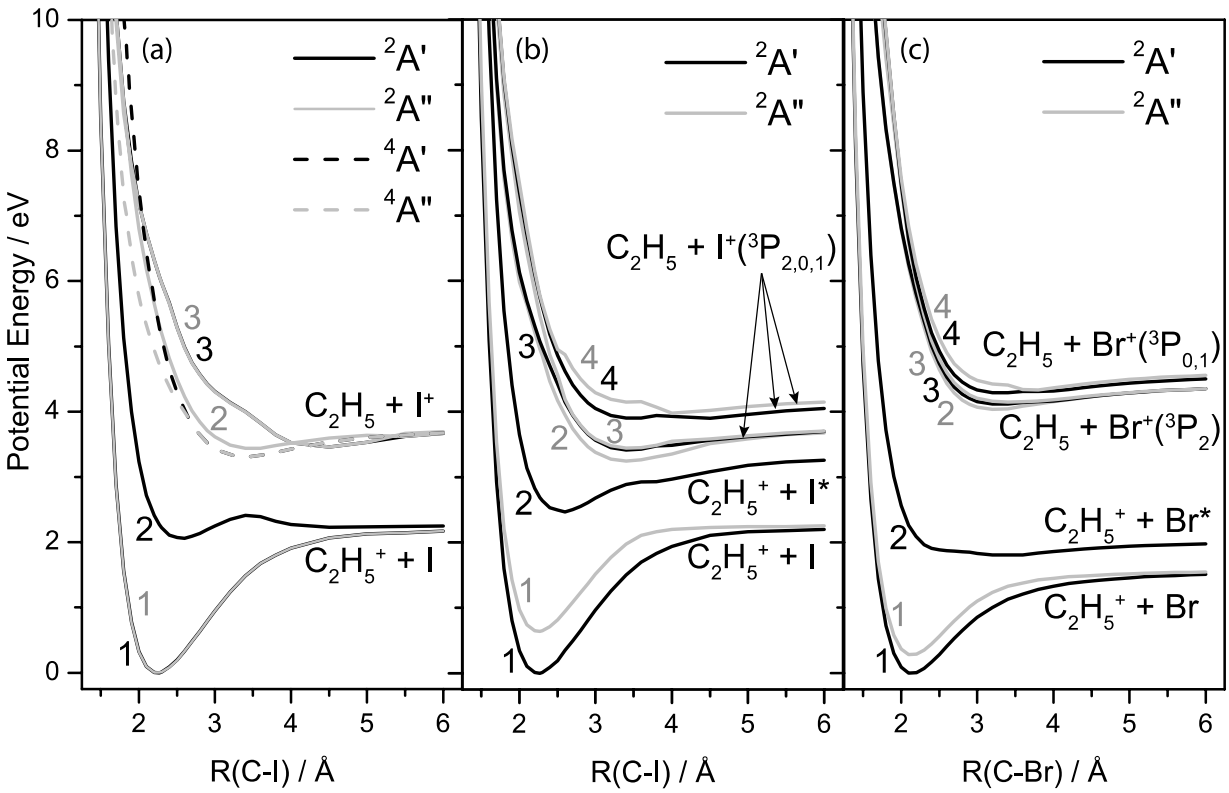

Figure 1 Calculated potential energy curves plotted as a function of C-X bond length for (a) $C_2H_5I^+$ (spin-orbit free), (b) $C_2H_5I^+$ (spin-orbit coupled), and (c) $C_2H_5Br^+$ (spin-orbit coupled). The energies shown are relative to that of the molecule in its ion ground state. Energies have been calculated every 0.1 Å along the C-X bond coordinate.

Possible transition states for HBr elimination from $C_2H_5Br^+$ were investigated using density functional theory (DFT) with the Becke 3-parameter exchange Lee Yang Parr (B3LYP) functional and the 6-311+(2*df*,*p*) Pople basis set within the Gaussian 09 computational package,[46] and optimised using the QST2 algorithm.

3. Results and Discussion

The spin-orbit-free PECs for $C_2H_5I^+$ returned by the CASPT2 rigid-body scans, shown in Figure 1(a), provide a convenient starting point for understanding the various excited states of the ethyl halide cations and their primary fragmentation mechanisms. In C_s symmetry, the ground 'state' is a $1^2A'/1^2A''$ pair (the analogue of the ^2E ground state of CH_3I^+). The first excited ($2^2A'$) PEC that correlates to the same $C_2H_5^+ + I$ limit is attributable to a $p_{x/y} \leftarrow \sigma$ promotion in the vertical Franck-Condon (vFC) region. All of the various doublet and quartet spin-orbit-free PECs correlating to the $C_2H_5 + I^+$ limit appear to be, at best, very weakly bound. Those shown in Figure 1(a) involve substantial contribution from $\sigma^* \leftarrow p_{x/y}$ promotion, and in the case of the long range part of the $3^2A'$ PEC, $\sigma^* \leftarrow \sigma$ promotions.

The corresponding spin-orbit coupled PECs for $C_2H_5I^+$ are shown in Figure 1(b), while the analogous spin-orbit-coupled PECs for $C_2H_5Br^+$ are shown in Figure 1(c). The first feature to note is the splitting of the 'ground' state into 1A′ and 1A″ PECs, which, by analogy with CH_3I^+ *etc*, have sometimes been termed $X_1{}^2E$ and $X_2{}^2E$ (see reference [51] and references therein). Both components of the ground state dissociate to ground-state $C_2H_5^+ + X$ products, with the 2A′ PEC correlating to $C_2H_5^+ + X^*$ products. A second feature is that the degeneracy of the $C_2H_5 + X^+$ asymptote in Figure 1(a) is lifted by the ^3P_J splitting of the X^+ ion. We return to consider these various PECs as and when required in the subsequent discussion.

3.1 Ethyl halide cation formation

Figure 2 shows energy level diagrams for the energetically accessible fragmentation channels of (a) $C_2H_5Br^+$ and (b) $C_2H_5I^+$ up to a total energy (defined relative to the zero-point level of the ground state neutral molecule) of ~16 eV. The energies of the ground state cations were taken from published mass-analysed threshold ionisation spectroscopy studies: C_2H_5I: IE(X_1A') = 9.3501(6) eV; IE(X_2A'') = 9.9334(6) eV;[51] C_2H_5Br: IE(X_1A') = 10.3040(6) eV; IE(X_2A'') = 10.5860(6) eV[52], where the value in parentheses represents the uncertainty in the final decimal place. The energies of the various product channels were estimated from available thermochemical data (*i.e.* ionisation energies (IE), appearance energies (AE), dissociation energies (*D*) and enthalpies of formation ($\Delta_f H$)) using appropriate Hess's Law cycles. The energies of the product channels, and the data used to determine these energies, are summarised in Table 1. We note that the spin-orbit-coupled calculations described in Section 2.2 are able to reproduce the relative strengths of the C–X^+ bonds in $C_2H_5I^+$ and $C_2H_5Br^+$ with good accuracy.

The $C_2H_5X^+$ cations in the present study are formed by 118 nm photoionization of the corresponding neutral molecule. As shown in Figure 2, the photon energy of 10.487 eV (84582 cm^{-1}) comfortably exceeds the first ionization energy (IE) of both ethyl halides. Given the non-bonding nature of the $p_{x/y}$ highest occupied molecular orbital (HOMO) in C_2H_5X, Franck-Condon arguments would suggest that 118 nm photoionization of the jet-cooled parent molecule will favour formation of $C_2H_5X^+$ ions in the ground ($v = 0$) vibrational level of the X_1A' (and X_2A'') states. This behaviour was suggested previously by Xu *et al.*[33], and is also consistent with the reported He I photoelectron spectrum.[53,54] The theoretical ranges of internal energies accessible to the nascent parent ions and to the excited-state ions created through absorption of a second 266 nm or 355 nm photon are indicated on Figure 2 by the shading above each energy level.

Table 1 Energies of the ground state $C_2H_5I^+$ and $C_2H_5Br^+$ parent cation and of the lower lying dissociation limits, referenced to the respective ground state neutral molecule in its zero-point vibrational level.

	ΔE (eV)	Source
$C_2H_5Br \rightarrow$		
$C_2H_5Br^+$ $X_1A'(X_2A'')$	10.30 (10.59)	IE(C_2H_5Br)[52]
$C_2H_5^+ + Br(Br^*)$	11.13 (11.59)	$AE_{0K}(C_2H_5^+)$,[31] S-O splitting[55]
$C_2H_3^+ + H_2 + Br(Br^*)$	13.24 (13.70)	$AE_{0K}(C_2H_5^+)$,[31] $D_0(C_2H_3^+\text{-}H_2)$,[56] S-O splitting[55]
$C_2H_4^+ + H + Br(Br^*)$	14.96 (15.41)	$AE_{0K}(C_2H_5^+)$,[31] IE(C_2H_5),[49] $D_0(C_2H_4\text{-}H)$,[56] IE(C_2H_4),[57] S-O splitting[55]
$C_2H_4^+ + HBr$	11.21	$AE_{0K}(C_2H_5^+)$,[31] IE(C_2H_5),[49] $D_0(C_2H_4\text{-}H)$,[56] IE(C_2H_4),[57] D_0(H-Br)[58]
$C_2H_4 + HBr^+$	12.37	$AE_{0K}(C_2H_5^+)$,[31] IE(C_2H_5),[49] $D_0(C_2H_4\text{-}H)$,[56] IE(HBr),[57] D_0(H-Br)[58]
$Br^+ + C_2H_5$	14.83	$AE_{0K}(C_2H_5^+)$,[31] IE(C_2H_5),[49] IE(Br)[55]
$Br^+ + C_2H_4 + H$	16.26	$AE_{0K}(C_2H_5^+)$,[31] IE(C_2H_5),[49] IE(Br),[55] $D_0(C_2H_4\text{-}H)$[56]
$CH_2Br^+ + CH_3$	12.41	$\Delta_f H_{0K}(CH_2I^+)$,[59] $\Delta_f H_{0K}(CH_3)$,[60] $\Delta_f H_{0K}(C_2H_5I)$[31]
$C_2H_5I \rightarrow$		
$C_2H_5I^+$ $X_1A'(X_2A'')$	9.35 (9.93)	IE(C_2H_5I)[51]
$C_2H_5^+ + I(I^*)$	10.53 (11.48)	$AE_{0K}(C_2H_5^+)$,[31] S-O splitting[55]
$C_2H_3^+ + H_2 + I(I^*)$	12.64 (13.59)	$AE_{0K}(C_2H_5^+)$,[31] $D_0(C_2H_3^+\text{-}H_2)$,[56] S-O splitting[55]
$C_2H_4^+ + H + I(I^*)$	14.36 (15.30)	$AE_{OK}(C_2H_5^+)$,[31] IE(C_2H_5),[49] $D_0(C_2H_4\text{-}H)$,[56] IE(C_2H_4),[57]
$C_2H_4^+ + HI$	11.30	$AE_{0K}(C_2H_5^+)$,[31] IE(C_2H_5),[49] $D_0(C_2H_4\text{-}H)$,[56] IE(C_2H_4),[57] D_0(H-I)[61]
$C_2H_4 + HI^+$	11.84	$AE_{0K}(C_2H_5^+)$,[31] IE(C_2H_5),[49] $D_0(C_2H_4\text{-}H)$,[56] IE(HI),[62] D_0(H-I)[61]
$I^+ + C_2H_5$	12.87	$AE_{0K}(C_2H_5^+)$,[31] IE(C_2H_5),[49] IE(I)[55]
$I^+ + C_2H_4 + H$	14.30	$AE_{0K}(C_2H_5^+)$,[31] IE(C_2H_5),[49] IE(I),[55] $D_0(C_2H_4\text{-}H)$[56]
$CH_2I^+ + CH_3$	12.10	$\Delta_f H_{0K}(CH_2I^+)$,[59] $\Delta_f H_{0K}(CH_3)$,[60] $\Delta_f H_{0K}(C_2H_5I)$[31]

3.2 Photofragmentation pathways of the ethyl halide cations

3.2.1 Fragment ion identification

The $C_2H_5Br^+$ and $C_2H_5I^+$ ions formed by 118 nm photoionization

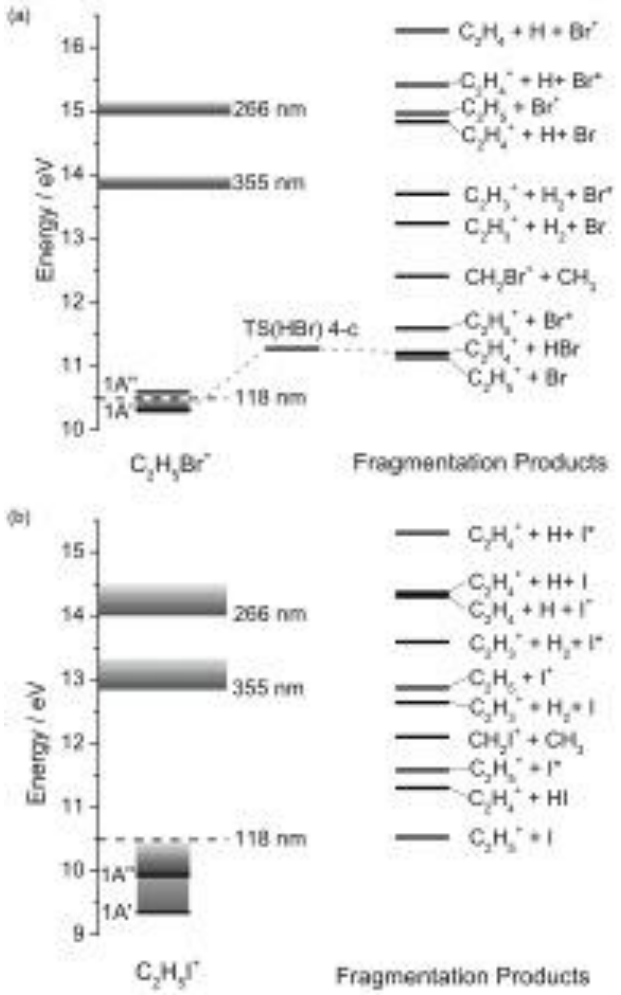

Figure 2 Energy level diagrams incorporating the lower lying dissociation pathways of (a) $C_2H_5Br^+$ and (b) $C_2H_5I^+$. The black horizontal levels indicate the electronic states of the $C_2H_5X^+$ parent ions. The black horizontal dashed lines indicate the energy of the 118 nm photon. The grey shaded regions, marked 355 nm and 266 nm, indicate approximately the region of the potential energy landscape to which the ions are excited on absorption of a UV photon of the wavelength indicated.

of the corresponding neutral molecules have been photolysed at 355 nm and 266 nm, with two additional wavelengths of 248 nm and 236 nm employed in the case of $C_2H_5I^+$. The measured product TOF mass spectra indicate formation of several different cation fragments, as illustrated in Figure 3 for photolysis of $C_2H_5Br^+$ and $C_2H_5I^+$ at both 355 nm and 266 nm.

Figure 3(a) shows that most of the fragment ion signal from UV photolysis of $C_2H_5Br^+$ falls in the mass range *m/z* 27-29. The ethyl ($C_2H_5^+$, *m/z* 29) and vinyl ($C_2H_3^+$, *m/z* 27) cation signals are slightly more intense than that of the ethene cation ($C_2H_4^+$, *m/z* 28) when exciting at 355 nm, at which wavelength we also detect a weak signal at *m/z* 93/95 attributable to the $CH_2{}^{79}Br^+$ / $CH_2{}^{81}Br^+$ cation (not shown here). The same fragment ions are detected when photolysing at 266 nm, but with differing peak intensities. The vinyl cation is a major fragmentation product at this wavelength, and ethyl ions appear to be a minor product. Additional fragment masses are also observed at this wavelength,

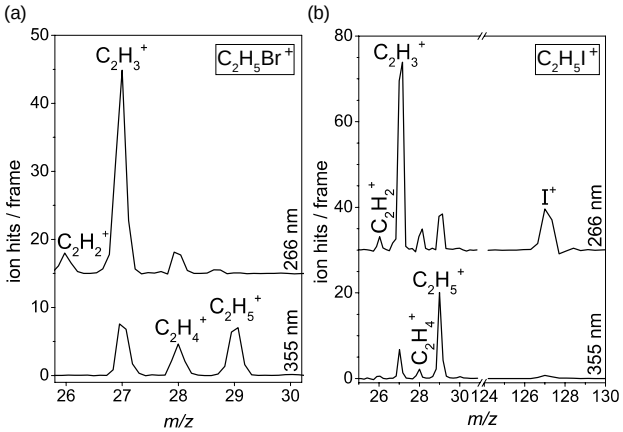

Figure 3 Time-of-flight mass spectra for the 355 nm and 266 nm photolysis products of (a) $C_2H_5Br^+$ and (b) $C_2H_5I^+$. The 266 nm traces for $C_2H_5Br^+$ and $C_2H_5I^+$ have been shifted vertically by 15 and 30 ion hits, respectively.

including the acetylene (or vinylidene) cation ($C_2H_2^+$, *m/z* 26) and CH_2^+ (*m/z* 14).

For the ethyl iodide cation (Figure 3(b)), 355 nm photolysis yields a mass spectrum dominated by ethyl cations (*m/z* 29), but smaller signals are also observed at *m/z* 26 ($C_2H_2^+$), 27 ($C_2H_3^+$), 28 ($C_2H_4^+$), 127 (I^+) and 141 (CH_2I^+, not shown here). At shorter wavelengths, $C_2H_3^+$ and I^+ signals dominate the TOF mass spectra, with the ethyl cation contributing little to the spectrum. The shoulder on the high mass side of the I^+ peak most probably corresponds to HI^+ (*m/z* 128).

To summarise, the TOF mass spectra indicate formation of $C_2H_3^+$, $C_2H_4^+$, $C_2H_5^+$ and CH_2X^+ products following UV photolysis of both $C_2H_5Br^+$ and $C_2H_5I^+$ cations and, in the latter case, I^+ ions also. Energetic considerations indicate that the weak $C_2H_2^+$ and CH_2^+ fragment ion signals must arise from multiphoton excitations involving at least one further UV photon. In this study, we focus on the one-photon dissociation pathways and, while the possible influence of multiphoton fragmentations on the measured primary ion signals must be considered, we will not attempt to unravel mechanistic details of the $C_2H_2^+$ and CH_2^+ formation processes.

3.2.2. Energetically accessible photofragmentation pathways

The following primary fragmentation channels are accessible to both $C_2H_5Br^+$ and $C_2H_5I^+$ cations within the range of photolysis wavelengths investigated.

(i) carbon-halogen (C–X) bond cleavage

$$C_2H_5X^+ \xrightarrow{h\nu} C_2H_5^+ + X \text{ (or } X^*) \qquad \text{Channel 1}$$

(ii) ethene cation production

$$C_2H_5X^+ \xrightarrow{h\nu} C_2H_4^+ + HX \qquad \text{Channel 2(a)}$$

$$\xrightarrow{h\nu} C_2H_4^+ + H + X \qquad \text{Channel 2(b)}$$

(iii) vinyl cation formation

$$C_2H_5X^+ \xrightarrow{h\nu} C_2H_3^+ + H_2 + X \text{ (or } X^*) \qquad \text{Channel 3}$$

(iv) carbon-carbon (C–C) bond cleavage

$$C_2H_5X^+ \xrightarrow{h\nu} CH_2X^+ + CH_3 \qquad \text{Channel 4}$$

As Figure 2 shows, a fifth dissociation channel, yielding I^+ products, is accessible in the case of $C_2H_5I^+$:

(v) C–X bond cleavage to produce X^+ cation

$$C_2H_5I^+ \xrightarrow{h\nu} C_2H_5 + I^+ \qquad \text{Channel 5}$$

The C–X bond cleavage (as in Channel 1), which is observed for both $C_2H_5Br^+$ and $C_2H_5I^+$, yields an ethyl cation along with a neutral halogen atom, which can be in either the ground (X) or spin-orbit excited (X*) states. The spin-orbit excited states lie at energies of 0.457 eV (Br*) and 0.943 eV (I*) above the respective ground states.[55]

Channel 5, involving C-X bond cleavage to yield an X^+ cation and a neutral ethyl radical, is observed in the case of $C_2H_5I^+$ when photolysing at 355 nm, but is not energetically accessible in the case of $C_2H_5Br^+$ at the photolysis wavelengths employed. As shown in Figure 1, several dissociative states of $C_2H_5I^+$ correlate with different spin-orbit components of the $C_2H_5 + I^+(^3P_J)$ limit, but the I^+ images recorded as part of the present study do not allow us to distinguish between these various limits.

There are two possible channels leading to $C_2H_4^+$ product formation. The first, Channel 2(a), involves concerted elimination of a neutral HX molecule. This is the lowest thermochemical threshold for forming $C_2H_4^+$, lying between the $C_2H_5^+ + X/X^*$ thresholds for both $C_2H_5Br^+$ and $C_2H_5I^+$ (Figure 2, and Table 1), and is accessible at the total energies investigated in this study. Such a process might feasibly occur from an excited state or, after internal conversion, from a high vibrational level of the ground state potential energy surface . An alternative sequential loss of X and H atoms, Channel 2(b), can also be envisaged, *e.g.* primary C–X bond fission, followed by subsequent H atom loss from a highly internally excited $C_2H_5^+$ co-fragment. However, reference to Figure 2 suggests that such a process might only contribute at the very shortest excitation wavelengths. We note that, in addition to the $C_2H_4^+ + HX$ channel, $C_2H_4 + HX^+$ products (with the charge residing on the HX rather than the C_2H_4 fragment) might also arise; indeed, Irsa[63] identified an appearance threshold of 11.7 eV for HI^+ products in an electron impact excitation study of C_2H_5I. As noted previously, the weak shoulder on the high *m*/*z* side of the I^+ peak in the TOF mass spectrum measured following UV photolysis of $C_2H_5I^+$ may indicate some contribution from this process, but this channel is not considered further in this study.

Vinyl cation production, Channel 3, could, in principle, arise via a concerted three-body fragmentation mechanism. However, a stepwise process, in which highly internally excited $C_2H_5^+$ cations formed via Channel 1 subsequently lose H_2, might appear more plausible.

C–C bond cleavage, Channel 4, was not considered in the earlier VMI study of $C_2H_5Br^+$ photolysis by Xu *et al.*,[33] but the present study shows evidence for CH_2X^+ product formation following UV photolysis of both $C_2H_5Br^+$ and $C_2H_5I^+$. Such a finding is fully consistent with the threshold energies of ~2.1 eV and ~2.8 eV for C–C bond fission in $C_2H_5Br^+$ and $C_2H_5I^+$, respectively (see **Table 1**).

The branching ratios for channels 1 to 5 vary both with parent cation and photolysis wavelength. In principle, relative branching ratios can be obtained directly from the fragment peak intensities in the TOF mass spectra, but such analyses are complicated by possible unimolecular decay of internally excited primary fragments (*e.g.* $C_2H_5^+$) and/or unintended multiphoton absorptions. Such complications will arguably be least problematic when using longer-wavelength (355 nm) photolysis photons. Following photolysis of $C_2H_5Br^+$ at this wavelength, the percentage ion yields for $C_2H_5^+$, $C_2H_3^+$, $C_2H_4^+$, and CH_2Br^+ are 41%, 38%, 20%, and 1%, respectively. The major fragmentation pathways therefore yield $C_2H_5^+$ and $C_2H_3^+$ cations, each accounting for ~40% of the total fragment ion signal, with $C_2H_4^+$ production accounting for most of the remainder. These conclusions are in good agreement with the earlier study of Xu *et al.*[33]. $CH_2Br^+ + CH_3$ products clearly constitute a minor channel, which was missed in the earlier study.[33]

The relative ion yields are considerably different following 355 nm photolysis of $C_2H_5I^+$, with percentage yields of 62%, 19%, 6%, 2%, and 12% for $C_2H_5^+$, $C_2H_3^+$, $C_2H_4^+$, CH_2I^+, and I^+, respectively. The $C_2H_5^+ + I$ channel is enhanced by around 50% relative to the corresponding process in $C_2H_5Br^+$, while the $C_2H_3^+ + H_2 + I$ channel is much less favoured. C–C bond fission (yielding $CH_2I^+ + CH_3$ fragments) is again a minor process, as is $C_2H_4^+$ ion formation. In contrast to $C_2H_5Br^+$, the $C_2H_5 + I^+$ Channel 5 is accessible upon 355 nm photolysis of $C_2H_5I^+$, yielding 12% of the total ion signal.

3.2.3 Photodissociation dynamics of $C_2H_5Br^+$

As noted in Section 2.1, velocity-map images were recorded for the more abundant fragment ions at the various UV wavelengths studied. The images yield: (i) the velocity distribution of each fragment ion, and thus the distribution of total translational energies, $P(E_T)$, associated with a given fragmentation channel; and (ii) the associated (velocity-dependent) spatial anisotropy parameters, β, which characterise the angular scattering distribution. Illustrative data sets, including the velocity-map images and $P(E_T)$ distributions for selected cation fragments from photolysis of $C_2H_5Br^+$ and $C_2H_5I^+$ are shown in Figures 4 and 5, respectively.

The $P(E_T)$ distributions derived from analysis of the $C_2H_5^+$ images from photolysis of $C_2H_5Br^+$ at 355 nm and 266 nm are displayed as blue and green traces in Figure 4(a). For each of the photolysis wavelengths studied, Table 2 lists:

1. The maximum total translational energy of the fragmentation products, E_T(max). This is calculated as the residual energy from the UV photon not consumed in breaking chemical bonds or forming electronically excited fragments. Two values are quoted in the table, E_T(max) and E_T(MAX), representing the two limiting cases in which the excess energy available from the ionization step is either carried away entirely as kinetic energy of the ionized electron (in which case the ion is formed in its ground electronic and vibrational state), or released entirely into internal energy of the nascent ion, respectively.

2. The mean fraction $\langle f_T \rangle$ of the available energy, E_T(max) (or E_T(MAX)) released into translation of the fragmentation products.

These values may be considered in light of the various available pathways to forming the observed dissociation products.

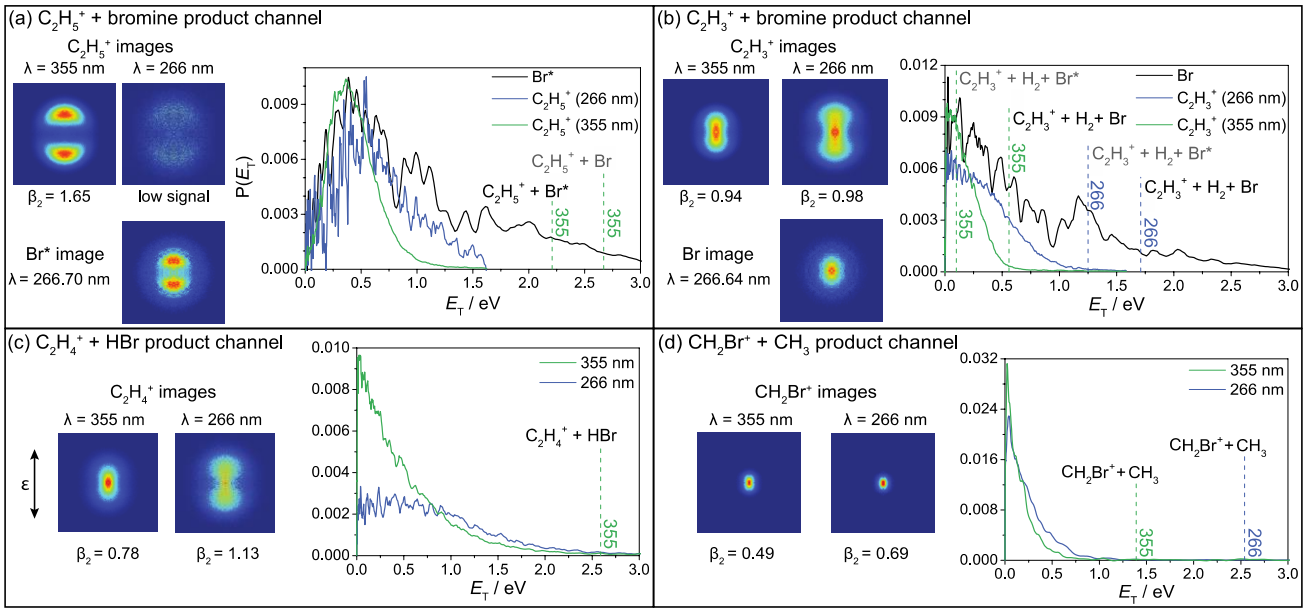

Figure 4 Total translational energy (E_T) distributions for the accessible product channels of $C_2H_5Br^+$ photolysis: (a) $C_2H_5^+$ + Br/Br*, (b) $C_2H_3^+$ + H_2 + Br, (c) $C_2H_4^+$ + HBr; and (d) CH_2Br^+ + CH_3. The $P(E_T)$ distributions derived from the velocity-map images of the ions produced following photolysis of $C_2H_5Br^+$ at 355 nm and 266 nm are displayed in green and blue, respectively. The vertical dashed lines indicate the maximum translational energy E_T(max) of the photofragments following photolysis at 355 nm (green) and 266 nm (blue). The E_T distributions for Br* and Br, detected using (2+1) REMPI, are plotted in black alongside the $C_2H_5^+$ and $C_2H_3^+$ data, in (a) and (b), respectively. The velocity-map images shown have been symmetrized for presentation purposes only.

The potential energy surfaces in Figure 1(c) imply that both 355 nm and 266 nm photoexcitation are likely to populate the 2A' excited state of the ion, with the experimental data indicating that this state can decay in at least two different ways.

The 2A' state is dissociative along the C–Br stretch coordinate, and correlates with $C_2H_5^+$ + Br* products. Miller and Baer [29] have previously postulated $C_2H_5^+$ formation via direct dissociation from the 2A' state, based on ion kinetic energy release distributions measured in a TPEPICO experiment, but were unable to measure the fragment angular distributions. Both the kinetic energy release and angular distributions measured for $C_2H_5^+$ in the present experiments support the previous conclusions of Miller and Baer[29]. The images shown in Figure 4(a) reveal an anisotropic E_T distribution peaking at $E_T > 0$. The near-limiting parallel recoil anisotropy ($\beta \sim 1.7$) indicates that the $C_2H_5^+$ products recoil along an axis parallel to the **ε** vector of the photolysing radiation, and therefore that the transition dipole moment for the excitation is directed along the breaking bond. This suggests that, as in the corresponding neutral, the parent excitation gains transition probability by mixing with the higher energy (3A′) state, which has substantial σ*←σ character.[14]

As shown in Table 2, when photolysing with 355 nm or 266 nm light, whether we assume that $C_2H_5^+$ is produced with a Br or Br* co-fragment, the mean translational energy, $\langle E_T \rangle$, is only around 15 % of E_T(max). The cation fragments must therefore be formed with substantial internal excitation, as noted previously by Xu *et al.*[33] The internal excitation results from the very different equilibrium geometries of the 2A′ and the X_1A'/X_2A'' states of the ion in coordinates other than the C–Br stretch coordinate plotted in Figure 1. This can be expected to give rise to conical intersections between the respective PESs, thereby facilitating efficient internal conversion to these latter states on a timescale comparable to that for excited state C–Br bond fission. Such pathways are expected to yield highly vibrationally excited $C_2H_5Br^+$ ions. At least some of these (see Figure 1) will evolve towards ground state $C_2H_5^+$ + Br products, with further fragmentation likely, of which more later.

Additional imaging studies of the Br/Br* atoms formed following photoexcitation of $C_2H_5Br^+$ at wavelengths ~266.6 nm (chosen to enable (2+1) REMPI detection of these atoms) were performed in an effort to use momentum matching of the Br/Br* and $C_2H_5^+$ images to determine the spin-orbit state of the bromine atoms partnering the $C_2H_5^+$ products. These experiments are complicated by the fact that 118 nm, 355 nm and 266.6 nm photons all pass through the interaction region, and that both of the latter wavelengths can photolyse $C_2H_5Br^+$ cations and thus contribute to the measured signal. For Br* and Br, the measured images are shown in Figure 4(a) and (b), respectively. The intense inner lobes of the Br* image, attributable to 355 nm photolysis of $C_2H_5Br^+$, display similar recoil anisotropy to that of the $C_2H_5^+$ fragments. The associated $P(E_T)$ distribution, derived assuming $C_2H_5^+$ co-fragments, is shown as the black line in Figure 4(a). It is dominated by a broad peak centred at E_T ~0.5 eV, and matches well with the $P(E_T)$ distributions obtained from the $C_2H_5^+$ images measured at both 355 nm and at 266 nm. We take this to indicate that the $C_2H_5^+$ fragments are formed with Br* co-products via direct dissociation from the 2A' state of $C_2H_5Br^+$. Note that the feature centred at E_T ~1 eV in Figure 4(a) arises from Br* products formed via photolysis of neutral (rather than cationic) ethyl bromide, and is not removed completely when subtracting the "266 nm only" signal. This has been verified through VMI studies of the neutral dissociation products in separate experiments – as reported also by Tang *et al.*[41] This feature is henceforth ignored when discussing the cation

fragmentation.

In contrast to the Br* data, the $P(E_T)$ distribution obtained from the *ground* state Br image, shown as a black line in Figure 4(b), peaks at $E_T < 0.1$ eV and does not compare well with the $P(E_T)$ distribution of the $C_2H_5^+$ fragments. Note that again the distribution of interest is contaminated by a "266 nm only" feature at E_T ~1.25 eV, which we have ignored in our analysis. While the kinetic energy release distributions for Br fragments cannot be momentum matched with those for $C_2H_5^+$, they are very similar to those for $C_2H_3^+$, shown in Figure 4(b). As noted earlier, a considerable proportion of $C_2H_5Br^+$ initially excited to the 2A' state is likely to undergo non-radiative decay to the ground state, yielding highly internally excited ions which then go on to dissociate into $C_2H_5^+$ and ground state Br. Since all of the observed $C_2H_5^+$ appears to be formed in coincidence with spin-orbit excited Br*, the $C_2H_5^+$ formed from ground state $C_2H_5Br^+$ must go on to fragment further, with $C_2H_3^+ + H_2$ being one possible channel. The low mass of the H_2 fragment means that the H_2 will carry away most of the kinetic energy released in the secondary dissociation step, such that the measured kinetic energy and angular distribution for the $C_2H_3^+$ fragment is likely to be very similar to that for the parent $C_2H_5^+$ cation. The observed momentum matching between the detected $C_2H_3^+$ ions and Br atoms provides considerable support for this proposed pathway. Further support is provided by the calculated maximum translational energies for the $C_2H_3^+ + H_2 + Br$ and $C_2H_3^+ + H_2 + Br^*$ products (assuming dissociation following excitation from the zero-point level of both spin-orbit states of the parent cation) shown in Figure 4(b) by two pairs of dashed vertical lines. The $P(E_T)$ distribution derived from the $C_2H_3^+$ image clearly extends beyond the maximum translational energy predicted for the $C_2H_3^+ + H_2 + Br^*$ channel, but tails off before the $C_2H_3^+ + H_2 + Br$ product limit. Thus, though we cannot completely exclude dissociation to $C_2H_3^+ + H_2 + Br^*$ products, we conclude that most of the $C_2H_3^+$ products are formed via a sequential three-body dissociation yielding H_2 and ground state Br atom co-fragments.

Images of the $C_2H_4^+$ fragment ions formed by photolysis at 355 nm and at 266 nm are shown in Figure 4(c). These products could arise via either a two-body or three-body dissociation process (*i.e.* HBr elimination or loss of H and Br atoms). As can be seen from Figure 2(a), a 355 nm photon provides insufficient energy for the three-body dissociation. Though energetically possible when exciting at 266 nm, the $P(E_T)$ distribution derived from the $C_2H_4^+$ images extends well beyond the maximum translation energy for the three body dissociation process. We can therefore discount this pathway, and focus on a pathway involving formation of HBr co-fragments, though these have not been directly detected. The $P(E_T)$ distributions for $C_2H_4^+$ produced following 266 nm and 355 nm photolysis both peak at or near zero, implying high levels of internal excitation in the products, ~90 % of E_T(max), and consistent with unimolecular decay on the ground state PES. The $C_2H_4^+$ images are anisotropic, with β ~0.8 for dissociation at 355 nm. This suggests that, as for $C_2H_3^+$ formation, the process of radiationless transfer to the ground state PES and subsequent HBr elimination occurs much faster than would be predicted by any purely statistical description of the dissociation process. While HBr elimination on the ground state PES could potentially occur via either a three-centre or a four-centre transition states, our DFT calculations have succeeded in locating a four-centre transition state lying ~1.05 eV above the potential minimum of the ground state cation. This backs up the conclusions from the earlier study of Xu *et al.*, who proposed a four-centre transition state based on data from experiments involving selective deuteration of the C_2H_5Br used to generate $C_2H_5Br^+$.[33]

The final fragmentation channel observed here, Channel 4, involves C–C bond fission and formation of $CH_2Br^+ + CH_3$ products. The CH_2Br^+ images measured following photolysis at 355 nm and 266 nm, shown in Figure 4(d), show low kinetic energy release, and mild anisotropy (β ~0.5). The $P(E_T)$ distributions derived from these images (Figure 4(d)) peak at zero, implying that the $CH_2Br^+ + CH_3$ products are also formed with high levels of internal excitation. Once again, this behaviour is understandable, qualitatively at least, in terms of non-statistical dissociation of internally 'hot' ground state molecules formed following radiationless transfer from the initially excited state after some pre-extension of the C–Br bond.

Table 2 Energetic parameters for the photofragmentation pathways of $C_2H_5Br^+$ calculated on the basis of the thermochemical data shown in Table 1: the maximum total kinetic energy, E_T(max); and the average

Fragmentation Products	λ / nm	E_T(max) (E_T(MAX)) / eV	$\langle f_T \rangle$
$C_2H_5^+ + Br$	355 nm	2.67 (2.85)	0.14 (0.13)
	266 nm	3.82 (4.01)	0.14 (0.13)
$C_2H_5^+ + Br^*$	355 nm	2.21 (2.40)	0.17 (0.16)
	266 nm	3.36 (3.55)	0.16 (0.15)
$C_2H_3^+ + H_2 + Br$	355 nm	0.56 (0.74)	0.22 (0.17)
	266 nm	1.71 (1.90)	0.14 (0.12)
$C_2H_3^+ + H_2 + Br^*$	355 nm	0.10 (0.29)	– (0.43)
	266 nm	1.25 (1.44)	0.19 (0.16)
$C_2H_4^+ + H + Br$	355 nm	– (–)	–
	266 nm	– (0.18)	–
$C_2H_4^+ + HBr$	355 nm	2.59 (2.77)	0.12 (0.11)
	266 nm	3.74 (3.93)	0.07 (0.07)
$C_2H_5 + Br^+$	355 nm	– (–)	Not observed
	266 nm	0.12 (0.31)	
$CH_2Br^+ + CH_3$	355 nm	1.39 (1.57)	0.10 (0.09)
	266 nm	2.54 (2.73)	0.07 (0.06)

fraction $\langle f_T \rangle$ of E_T(max) that goes into product translational energy.

3.2.4 Photodissociation dynamics of $C_2H_5I^+$

The images shown in Figure 5 of the various ions resulting from photolysis of $C_2H_5I^+$ reveal similarities, but also some differences between the fragmentation dynamics of $C_2H_5I^+$ and $C_2H_5Br^+$. The spin-orbit-coupled potential energy curves shown in Figure 1(b), and the energy level diagram shown in Figure 2(b), suggest that excited states correlating not just to $C_2H_5^+$ but also I^+ products should be energetically accessible at all of the UV wavelengths of present interest. This is confirmed by the fragment ion TOF mass

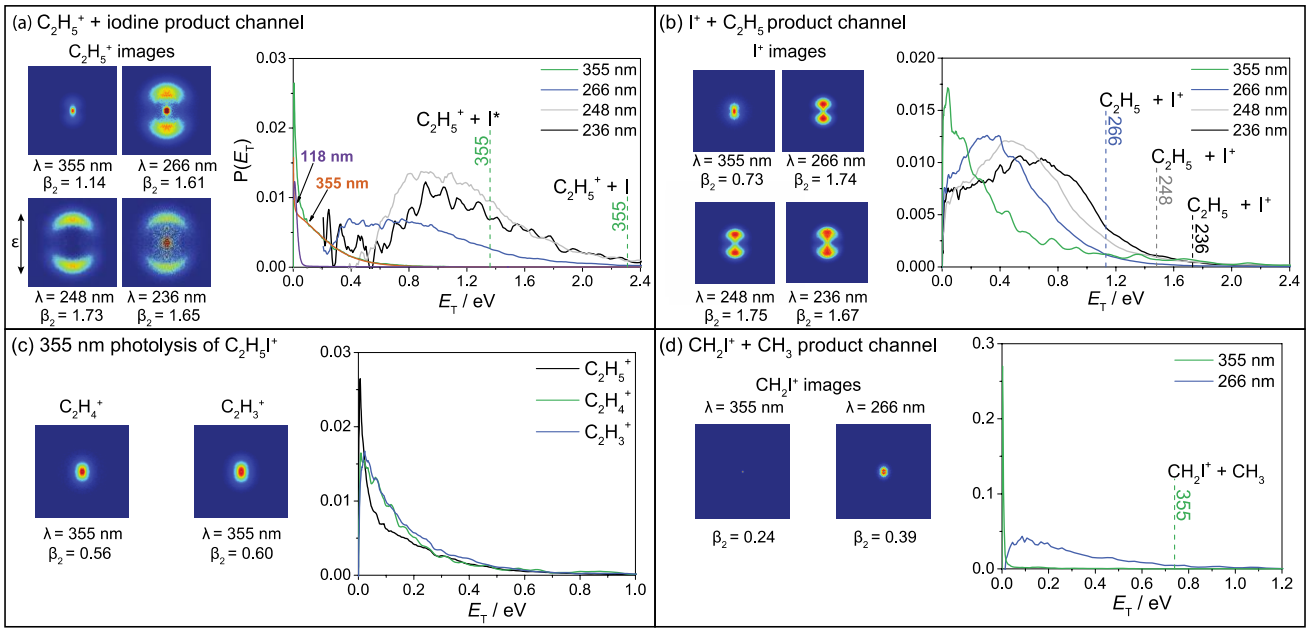

Figure 5 Total translational energy $P(E_T)$ distributions for the accessible product channels of $C_2H_5I^+$ photolysis: (a) $C_2H_5^+$ + I/I* at all four photolysis wavelengths; (b) C_2H_5 + I^+ at all four photolysis wavelengths; (c) $C_2H_5^+$ + I/I* (black), $C_2H_4^+$ + HI (green) and $C_2H_3^+$ + H_2 + I (blue) at 355 nm; and (d) CH_2I^+ + CH_3 at 355nm and 266 nm. The maximum translational energy E_T(max) are indicated by vertical dashed lines in the cases where they fall within the E_T scale shown. The velocity-map images shown have been symmetrized for presentation purposes only.

spectra shown in Figure 3(b) and by the images shown in Figures 5(a) and 5(b). E_T(max) and $\langle f_T \rangle$ values for the various photofragmentation channels are listed in Table 3.

The $C_2H_5^+$ image obtained following 355 nm photolysis of $C_2H_5I^+$ is obviously very different from that obtained for $C_2H_5Br^+$. The ion velocities are very low, with the kinetic energy release distribution peaking at zero and extending to E_T ~0.8 eV. The 118 nm photon used to generate $C_2H_5I^+$ provides just sufficient energy to cause dissociative ionization to $C_2H_5^+$ + I products. This channel is visible as the central spot in the $C_2H_5^+$ image and the associated spike at E_T = 0 in the $P(E_T)$ distribution. The remainder of the $C_2H_5I^+$ ions undergo 355 nm photolysis, yielding the tail of the $P(E_T)$ distribution extending to E_T ~0.8 eV. The two contributions can be separated approximately by fitting the distributions to a sum of two Gaussians, and are shown in purple and orange, respectively, in Figure 5(a).

A translational energy of E_T ~0.8 eV is far below the maximum permitted by energy conservation, even if the atomic co-fragments are formed in the spin-orbit-excited I* state, so it is clear that $C_2H_5^+$ ions are formed with a high degree of internal excitation. Extracting a reliable β parameter from the data is hampered by the small size of the image, but our best analysis suggests β ~ 1.2.

The data for 355 nm photolysis should be contrasted with the $C_2H_5^+$ images recorded at 266, 248 and 236 nm, also shown in Figure 5(a), all of which show an anisotropic distribution of fast products (characterised by β ~ 1.6-1.7) and $P(E_T)$ distributions that peak progressively further from E_T = 0 [note that in some cases, subtraction of the 118/355 nm signal is imperfect, and a small residual central spot remains, arising from dissociative ionization at 118 nm]. The observed anisotropy is most plausibly explained by initial excitation to the 3A′ and/or 4A′ (σσ*) states (see Figure 1), followed by diabatic dissociation via radiationless transfer through a conical intersection to $C_2H_5^+$ + I* products. Attempts to use (2+1)REMPI to detect I/I* products from 266 nm photolysis of $C_2H_5I^+$ were thwarted by the large 266 nm laser induced I^+ yield.

Two other features of these two-laser images merit note. As in the case of $C_2H_5Br^+$, the $P(E_T)$ distributions peak well below the maximum E_T value allowed by energy conservation, implying substantial internal excitation of the fragment cation. This is consistent with the large change in equilibrium geometry of the C_2H_5 moiety on dissociation. Secondly, the $P(E_T)$ distribution determined at 266 nm (Figure 5(a)) appears bimodal, and the TOF mass spectrum recorded when exciting at this wavelength (Figure 3(b)) shows a substantial I^+ yield, implying a major role for the C_2H_5 + I^+ fragmentation channel. Tang *et al.*[32] have demonstrated efficient (1+1)REMPI of neutral C_2H_5 fragments (via the 3*s* Rydberg state[64]) in this wavelength region, which gives an additional contribution to the $C_2H_5^+$ image. Comparison of the $P(E_T)$ distributions derived from the $C_2H_5^+$ and I^+ images suggests that the shoulder at E_T ~0.4 eV in Figure 5(a) is attributable to 266 nm two-photon ionization of neutral ethyl radicals from the C_2H_5 + I^+ pathway, while the peak at E_T ~0.8 eV is associated with $C_2H_5^+$ + I product formation.

The I^+ images obtained at all four photolysis wavelengths, shown in Figure 5(b), are markedly different from those of the $C_2H_5^+$ fragments shown in Figure 5(a). Therefore, we can confirm that the observed I^+ does not originate from the neutral iodine formed as the co-fragment to $C_2H_5^+$. The images measured at the three shorter wavelengths are clearly anisotropic (β ~ 1.7) and the derived $P(E_T)$ distributions (Figure 5(b)), the extent of which can be fully understood if we consider initial population of the 1A″ state of $C_2H_5I^+$, all peak at E_T > 0. Such energy disposal is very

reminiscent of that observed for the $C_2H_5^+$ product ions at these wavelengths, and can be explained in the same way – *i.e.* photoexcitation to the 3A′ and/or 4A′(σσ*) states and prompt dissociation to (in this case) the adiabatic products $C_2H_5 + I^+$. The 355 nm I^+ data is also reminiscent of that seen when monitoring $C_2H_5^+$ fragment ions. The recoil velocity distribution is more isotropic (β ~ 0.7), and the $P(E_T)$ distribution peaks at E_T = 0 but extends out to the maximum accessible translational energy. The 355 nm data for both $C_2H_5^+$ and I^+ may be explained by near-threshold excitation to the lowest adiabatic potential correlating to I^+ products, 3A′, followed by dissociation either to $C_2H_5 + I^+$ or, following non-adiabatic population transfer, to $C_2H_5^+ + I$ products.

Both $C_2H_3^+$ and $C_2H_4^+$ fragment ions are observed at all four photolysis wavelengths investigated. Images recorded following 355 nm photolysis are shown in Figure 5(c), along with a comparison of the $P(E_T)$ distributions derived for the $C_2H_5^+$, $C_2H_4^+$ and $C_2H_3^+$ ions. As noted earlier, we were unfortunately unable to employ REMPI detection of the I and I* products in order to determine their coproducts via momentum matching, and our discussion of possible $C_2H_3^+$ (and $C_2H_4^+$) formation routes is therefore guided by energetic considerations.

As noted above, $C_2H_5^+$ fragments are formed via two mechanisms: near-threshold dissociative ionization of C_2H_5I at 118 nm; and photolysis of nascent $C_2H_5I^+$ from the 118 nm photoionization step following absorption of a second, longer wavelength, photon. $C_2H_3^+$ ions may be formed either through photodissociation of the internally cold $C_2H_5^+$ formed in the former process, or through spontaneous secondary dissociation of the internally hot $C_2H_5^+$ formed in the latter process, as was observed following $C_2H_5Br^+$ photolysis. Since the kinetic energy release distribution for $C_2H_3^+$ from $C_2H_5I^+$ is very reminiscent of the analogous distribution following $C_2H_5Br^+$ photolysis, we suggest that the latter mechanism most probably dominates.

Photolysis of $C_2H_5^+$ fragments arising from 118 nm dissociative photoionization of C_2H_5I could also contribute to the observed $C_2H_4^+$ ion yield at 266, 248 and 236 nm. Again, we focus on the data from 355 nm photolysis. The threshold energy for three-body dissociation to $C_2H_4^+ + H + I$ products (4.94 eV or 4.36 eV when defined relative to the X_1A′ and X_2A″ states of the $C_2H_5I^+$ cation, respectively) is too high for parent ion photolysis to be a feasible route to $C_2H_4^+$ fragments at 355 nm, but the alternative HI elimination channel, the analogue of that proposed to account for HBr formation in the case of $C_2H_5Br^+$ photolysis, appears eminently plausible. As was the case for $C_2H_5Br^+$, the average translational energies, $\langle E_T \rangle$, derived from the $C_2H_4^+$ fragment ion images increase as the excitation wavelength is reduced, and the bulk of the available energy, ~90 % of E_T(max), is partitioned into product internal excitation. Both of these features are consistent with unimolecular decay of internally 'hot' parent molecules following radiationless transfer to the ground state PES. Previously, Baer *et al.*[28] measured an energetic threshold for formation of $C_2H_4^+$ that was significantly higher than predicted from thermochemical data, and was consistent with the presence of an energy barrier along the dissociation coordinate. As noted earlier (see Section 3.2.3), in the case of $C_2H_5Br^+$ dissociation to form $C_2H_4^+$, a transition state was indeed located along this pathway, lying ~0.14 eV higher in energy than the products. We have not searched for the analogous transition state in $C_2H_5I^+$, but a barrier similar in magnitude to that in $C_2H_5Br^+$ lies well below the photon energies employed in this study, and is unlikely to have a significant effect on the measured translational energy release distributions.

Table 3 Energetic parameters for the photofragmentation pathways of $C_2H_5I^+$ calculated on the basis of the thermochemical data shown in Table 1: the maximum total kinetic energy, E_T(max); and the average fraction $\langle f_T \rangle$ of E_T(max) that goes into translational energy.

Fragmentation Products	λ / nm	E_T(max) (E_T(MAX)) / eV	$\langle f_T \rangle$
$C_2H_5^+ + I$	355 nm	2.31 (3.45)	0.09 (0.06)
	266 nm	3.47 (4.61)	0.29 (0.21)
	248 nm	3.82 (4.96)	0.30 (0.23)
	236 nm	4.07 (5.21)	0.30 (0.23)
$C_2H_5^+ + I^*$	355 nm	1.36 (2.50)	0.15 (0.08)
	266 nm	2.52 (3.66)	0.39 (0.27)
	248 nm	2.87 (4.01)	0.39 (0.28)
	236 nm	3.12 (4.26)	0.39 (0.29)
$C_2H_3^+ + H_2 + I$	355 nm	0.20 (1.34)	0.62 (0.09)
	266 nm	1.36 (2.50)	0.13 (0.07)
	248 nm	1.71 (2.85)	0.12 (0.07)
	236 nm	1.96 (3.10)	0.11 (0.07)
$C_2H_3^+ + H_2 + I^*$	355 nm	– (0.39)	– (0.32)
	266 nm	0.41 (1.55)	0.44 (0.12)
	248 nm	0.76 (1.90)	0.26 (0.11)
	236 nm	1.01 (2.15)	0.21 (0.10)
$C_2H_4^+ + H + I$	355 nm	– (–)	– (–)
	266 nm	– (0.78)	– (0.26)
	248 nm	– (1.13)	– (0.23)
	236 nm	0.24 (1.38)	– (0.20)
$C_2H_4^+ + HI$	355 nm	1.54 (2.68)	0.09 (0.05)
	266 nm	2.70 (3.84)	0.08 (0.05)
	248 nm	3.05 (4.19)	0.09 (0.06)
	236 nm	3.30 (4.44)	0.08 (0.06)
$C_2H_5 + I^+$	355 nm	- (1.11)	- (0.23)
	266 nm	1.13 (2.27)	0.30 (0.15)
	248 nm	1.48 (2.62)	0.34 (0.19)
	236 nm	1.73 (2.87)	0.35 (0.21)
$CH_2I^+ + CH_3$	355 nm	0.74 (1.88)	0.07 (0.03)
	266 nm	1.90 (3.04)	0.23 (0.14)
	248 nm	2.25 (3.39)	Not observed
	236 nm	2.50 (3.64)	

Figure 5(d) shows images of the CH_2I^+ products formed via the C–C bond fission channel following excitation of $C_2H_5I^+$ at 355 and 266 nm. The $P(E_T)$ distribution in the former case is very narrow – more so than in the case of $C_2H_5Br^+$ – and peaks at E_T = 0. Moving to shorter excitation wavelengths (*e.g.* 266 nm)

results in a CH_2I^+ image with a larger radius and a $P(E_T)$ distribution which peaks a little above zero and extends to higher E_T, but still stops well short of the E_T(max) value for $CH_2I^+ + CH_3$ products. As in the case of the $C_2H_4^+$ products, such energy disposal is most readily understood in terms of unimolecular decay of internally excited ground-state $C_2H_5I^+$ cations.

4. Conclusions

We have presented a comprehensive velocity-map imaging study into the various photofragmentation pathways of the $C_2H_5Br^+$ and $C_2H_5I^+$ cations at a range of wavelengths in the UV. Interpretation of the data is aided by reference to high-level spin-orbit-resolved *ab initio* potential energy curves along the R(C–X) coordinate for the lowest few electronic states of both cations. The present results corroborate and substantially extend the knowledge gained from previous experimental studies of the title cations [28,29,33].

In the case of $C_2H_5Br^+$, 266 nm or 355 nm excitation to the 2A' state results in competition between direct dissociation from this state to yield $C_2H_5^+ + Br^*$, and radiationless decay to form highly vibrationally excited ground-state $C_2H_5Br^+$. The latter can decay via a variety of mechanisms to form $C_2H_5^+ + Br$ (with a high degree of internal excitation in the ethyl ion), $C_2H_4^+ + HBr$, or $CH_3 + CH_2Br^+$. The $C_2H_5^+$ formed in the first of these pathways dissociates further to form $C_2H_3^+$. In all cases the available energy is preferentially partitioned into internal excitation of the products.

$C_2H_5I^+$ photolysis at 355 nm, 266 nm, 248 nm and 236 nm yields fragment ions analogous to those from $C_2H_5Br^+$ (*i.e.* $C_2H_5^+$, $C_2H_4^+$, $C_2H_3^+$ and CH_2I^+), with the additional detection of I^+ ions indicating that the $C_2H_5 + I^+$ channel is open at all four wavelengths studied, in agreement with the predictions of the *ab initio* calculations. The images and $P(E_T)$ distributions suggest that the dynamics leading to formation of $C_2H_5^+$, $C_2H_4^+$, $C_2H_3^+$, and CH_2I^+ share many similarities with those for the analogous fragmentation channels in $C_2H_5Br^+$. However, definitive interpretation of the data is hampered somewhat by the much greater possible spread of energies in the parent cations formed upon VUV photoionization and our inability to carry out separate imaging measurements on the neutral I/I* fragments.

Acknowledgements

The authors gratefully acknowledge funding from the ERC through Starting Independent Researcher Grant 200733 'ImageMS' (to CV), the EPSRC (Programme Grant EP/G00224X/1) and the Marie Curie Initial Training Network 238671 'ICONIC'. The Bristol authors are most grateful to Prof J.N. Harvey and Dr A.M. Wenge for many useful discussions.

References

1. M. Shapiro and R. Bersohn, *J. Chem. Phys.*, 1980, **73**, 3810–3817.
2. R. K. Sparks, K. Shobatake, L. R. Carlson, and Y. T. Lee, *J. Chem. Phys.*, 1981, **75**, 3838–3846.
3. M. D. Barry and P. A. Gorry, *Mol. Phys.*, 1984, **52**, 461–473.
4. J. F. Black and I. Powis, *Chem. Phys.*, 1988, **125**, 375–388.
5. I. Powis and J. F. Black, *J. Phys. Chem.*, 1989, **93**, 2461–2470.
6. S. J. Riley and K. R. Wilson, *Faraday Discuss.*, 1972, **53**, 132–146.
7. G. Van Veen, T. Baller, A. E. De Vries, and N. Van Veen, *Chem. Phys.*, 1984, **87**, 405–417.
8. D. W. Chandler and P. L. Houston, *J. Chem. Phys.*, 1987, **87**, 1445–1447.
9. F. G. Godwin, P. A. Gorry, P. M. Hughes, D. Raybone, T. M. Watkinson, and J. C. Whitehead, *Chem. Phys. Lett.*, 1987, **135**, 163–169.
10. R. de Nalda, J. Durá, G. A. Garcia, J. G. Izquierdo, J. González-Vázquez, and L. Bañares, *J. Chem. Phys.*, 2008, **128**, 244309.
11. A. T. J. B. Eppink and D. H. Parker, *J. Chem. Phys.*, 1998, **109**, 4758.
12. D. W. Chandler, J. W Thoman Jr., M. H. M. Janssen, and D. H. Parker, *Chem. Phys. Lett.*, 1989, **156**, 151–158.
13. A. T. J. B. Eppink and D. H. Parker, *J. Chem. Phys.*, 1999, **110**, 832–844.
14. A. B. Alekseyev, H.-P. Liebermann, R. J. Buenker, and S. N. Yurchenko, *J. Chem. Phys.*, 2007, **126**, 234102.
15. Y. Amatatsu, S. Yabushita, and K. Morokuma, *J. Chem. Phys.*, 1996, **104**, 9783–9794.
16. A. I. Chichinin, K. H. Gericke, S. Kauczok, and C. Maul, *Int. Rev. Phys. Chem.*, 2009, **28**, 607–680.
17. B. P. Tsai, T. Baer, A. S. Werner, and S. F. Lin, *J. Phys. Chem.*, 1975, **79**, 570–574.
18. D. M. Mintz, *J. Chem. Phys.*, 1976, **65**, 2407–2415.
19. J. H. D. Eland, R. Frey, A. Kuestler, H. Schulte, and B. Brehm, *Int. J. Mass Spectrom. Ion Phys.*, 1976, **22**, 155–170.
20. Y. J. Bae and M. S. Kim, *J. Chem. Phys.*, 2008, **128**, 124324.
21. Y. J. Bae and M. S. Kim, *ChemPhysChem*, 2008, **9**, 1709–1714.
22. A. Bodi, N. S. Shuman, and T. Baer, *Phys. Chem. Chem. Phys.*, 2009, **11**, 11013–11021.
23. V. Blanchet, P. C. Samartzis, and A. M. Wodtke, *J. Chem. Phys.*, 2009, **130**, 034304.
24. M. Kawasaki, H. Sato, T. Kikuchi, R. Kobayashi, and T. Arikawa, *J. Chem. Phys.*, 1987, **87**, 5739–5745.
25. T. Gougousi, P. C. Samartzis, and T. N. Kitsopoulos, *J. Chem. Phys.*, 1998, **108**, 5742–5746.
26. D. Townsend, S. K. Lee, and A. G. Suits, *J. Phys. Chem. A*, 2004, 8106–8114.
27. R. Locht, D. Dehareng, K. Hottmann, H. W. Jochims, H. Baumgärtel, and B. Leyh, *J. Phys. B*, 2010, **43**, 105101.
28. T. Baer, U. Buchler, and C. E. Klots, *J. Chim. Phys.*, 1980, **77**, 739–743.
29. B. E. Miller and T. Baer, *Chem. Phys.*, 1984, **85**, 39–45.
30. T. Baer, Y. Song, J. Liu, W. Chen, and C. Y. Ng, *Faraday Discuss.*, 2000, **115**, 137–145.
31. S. Borkar and B. Sztáray, *J. Phys. Chem. A*, 2010, **114**, 6117–6123.
32. Y. Tang, W.-B. Lee, Z. Hu, B. Zhang, and K.-C. Lin, *J. Chem. Phys.*, 2007, **126**, 064302.
33. D. Xu, R. J. Price, J. Huang, and W. M. Jackson, *Z. Phys. Chem.*, 2001, **215**, 253–271.
34. K. Suto, Y. Sato, C. L. Reed, V. Skorokhodov, Y. Matsumi, and M. Kawasaki, *J. Phys. Chem. A*, 1997, **101**, 1222–1226.
35. W. S. Hopkins, M. L. Lipciuc, S. H. Gardiner, and C. Vallance, *J. Chem. Phys.*, 2011, **135**, 034308.
36. A. H. Kung, J. F. Young, and S. E. Harris, *Appl. Phys. Lett.*, 1973, **22**, 301–302.
37. A. H. Kung, J. F. Young, and S. E. Harris, *Appl. Phys. Lett.*, 1976, **28**, 294.
38. G. Bjorklund, *IEEE J. Quantum Electron.*, 1975, **11**, 287–296.
39. R. Mahon, T. J. McIlrath, V. P. Myerscough, and D. W. Koopman, *IEEE J. Quantum Electron.*, 1979, **15**, 444–451.
40. B. Tang, R. Zhu, Y. Tang, L. Ji, and B. Zhang, *Chem. Phys.*, 2004, **303**, 37–42.
41. Y. Tang, L. Ji, R. Zhu, Z. Wei, and B. Zhang, *ChemPhysChem*, 2005, **6**, 2137–2144.
42. A. I. Chichinin, *J. Phys. Chem. Ref. Data*, 2006, **352**, 869–928.
43. R. Zhu, B. Tang, L. Ji, Y. Tang, S. Zhang, and B. Zhang, *Opt. Commun.*, 2004, **235**, 325–331.
44. Y. Tang, L. Ji, B. Tang, R. Zhu, S. Zhang, and B. Zhang, *Chem. Phys. Lett.*, 2004, **392**, 493–497.

45. G. M. Roberts, J. L. Nixon, J. Lecointre, E. Wrede, and J. R. R. Verlet, *Rev. Sci. Instrum.*, 2009, **80**, 053104.
46. M. J. Frisch, G. W. Trucks, H. B. Schlegel, G. E. Scuseria, M. A. Robb, J. R. Cheeseman, G. Scalmani, V. Barone, B. Mennucci, G. A. Petersson, H. Nakatsuji, M. Caricato, X. Li, H. P. Hratchian, A. F. Izmaylov, J. Bloino, G. Zheng, J. L. Sonnenberg, M. Hada, M. Ehara, K. Toyota, R. Fukuda, J. Hasegawa, M. Ishida, T. Nakajima, Y. Honda, O. Kitao, H. Nakai, T. Vreven, J. A. Montgomery, J. E. Peralta, F. Ogliaro, M. Bearpark, J. J. Heyd, E. Brothers, K. N. Kudin, V. N. Staroverov, R. Kobayashi, J. Normand, K. Raghavachari, A. Rendell, J. C. Burant, S. S. Iyengar, J. Tomasi, M. Cossi, N. Rega, J. M. Millam, M. Klene, J. E. Knox, J. B. Cross, V. Bakken, C. Adamo, J. Jaramillo, R. Gomperts, R. E. Stratmann, O. Yazyev, A. J. Austin, R. Cammi, C. Pomelli, J. W. Ochterski, R. L. Martin, K. Morokuma, V. G. Zakrzewski, G. A. Voth, P. Salvador, J. J. Dannenberg, S. Dapprich, A. D. Daniels, Farkas, J. B. Foresman, J. V. Ortiz, J. Cioslowski, and D. J. Fox, *Gaussian 09, Revision B.01*, 2009.
47. M. Dolg, *Habilitationsschrift*, Universität Stuttgart, 1997.
48. K. A. Peterson, B. C. Shepler, D. Figgen, and H. Stoll, *J. Phys. Chem. A*, 2006, **110**, 13877–13883.
49. B. Ruscic, J. Berkowitz, L. A. Curtiss, and J. A. Pople, *J. Chem. Phys.*, 1989, **91**, 114.
50. H.-S. Andrei, N. Solcà, and O. Dopfer, *Angew. Chem. Int. Ed.*, 2008, **47**, 395–397.
51. N. Knoblauch, A. Strobel, I. Fischer, and V. E. Bondybey, *J. Chem. Phys.*, 1995, **103**, 5417–5427.
52. B. Tang, S. Zhang, Y. Wang, Y. Tang, and B. Zhang, *J. Chem. Phys.*, 2005, **123**, 164305.
53. A. Giuliani, F. Motte-Tollet, J. Delwiche, N. J. Mason, N. C. Jones, J. M. Gingell, I. C. Walker, and M. J. Hubin-Franskin, *J. Chem. Phys.*, 2000, **112**, 6285.
54. A. Giuliani, F. Motte-Tollet, J. Delwiche, J. Heinesch, N. J. Mason, J. M. Gingell, I. C. Walker, N. C. Jones, and M. J. Hubin-Franskin, *J. Chem. Phys.*, 1999, **110**, 10307–10315.
55. A. Kramida, Y. Ralchenko, J. Reader, and A. T. NIST, *NIST Atomic Spectra Database (ver. 5.0), [Online]. Available: http://physics.nist.gov/asd [August 23]*, 2013.
56. H. Fan and S. T. Pratt, *J. Chem. Phys.*, 2005, **123**, 204301.
57. S. Willitsch, U. Hollenstein, and F. Merkt, *J. Chem. Phys.*, 2004, **120**, 1761–1774.
58. P. M. Regan, S. R. Langford, A. J. Orr-Ewing, and M. N. R. Ashfold, *J. Chem. Phys.*, 1999, **110**, 281–288.
59. A. F. Lago, J. P. Kercher, A. Bodi, B. Sztáray, B. Miller, D. Wurzelmann, and T. Baer, *J. Phys. Chem. A*, 2005, **109**, 1802–1809.
60. B. Ruscic, J. E. Boggs, A. Burcat, and A. G. Császár, *J. Phys. Chem. Ref. Data*, 2005, **34**, 573–656.
61. S. R. Langford, P. M. Regan, A. J. Orr-Ewing, and M. N. R. Ashfold, *Chem. Phys.*, 1998, **231**, 245–260.
62. S. T. Pratt, *J. Chem. Phys.*, 1994, **101**, 8302–8309.
63. A. P. Irsa, *J. Chem. Phys.*, 1957, **26**, 18–22.
64. H. R. Wendt and H. E. Hunziker, *J. Chem. Phys.*, 1984, **81**, 717–723.